JGR Biogeosciences

RESEARCH ARTICLE
10.1029/2026JG009780

Mixo-COBALT: Incorporating Plastic Mixotrophy Into a Coupled Biogeochemical Ocean Model in the Sargasso Sea

Alan D. Sheu[1], **Jessica Y. Luo**[2], **Kevin M. Archibald**[1], **and Holly V. Moeller**[1]

[1]Department of Evolution, Ecology, and Marine Biology, University of California, Santa Barbara, Santa Barbara, CA, USA, [2]Geophysical Fluid Dynamics Laboratory, National Oceanic and Atmospheric Administration, Princeton, NJ, USA

Key Points:

- We implemented a phenotypically plastic mixotroph into a coupled biogeochemical ocean model
- Acclimation was largely light-driven, with phototrophy and phagotrophy dominant in shallow and deep mixed layers respectively
- Increased mixotroph bacterivory led to higher turnover rates, trophic efficiency, and carbon export

Supporting Information:

Supporting Information may be found in the online version of this article.

Correspondence to:

A. D. Sheu,
adsheu@ucsb.edu

Citation:

Sheu, A. D., Luo, J. Y., Archibald, K. M., & Moeller, H. V. (2026). Mixo-COBALT: Incorporating plastic mixotrophy into a coupled biogeochemical ocean model in the Sargasso Sea. *Journal of Geophysical Research: Biogeosciences*, *131*, e2026JG009780. https://doi.org/10.1029/2026JG009780

Received 17 FEB 2026
Accepted 30 JUL 2026

Abstract Mixotrophic plankton incorporate both autotrophy (via photosynthesis) and heterotrophy (via phagotrophic grazing) into their metabolism. A large portion of marine protists are likely mixotrophic, significantly contributing to bacterivory and regulating biogeochemical cycling. Constitutive mixotrophs that produce their own plastids are often phenotypically plastic, varying their relative investments in photosynthesis and grazing depending on environmental conditions. However, plastic mixotrophs have yet to be implemented into a large-scale coupled ocean model. Thus, we incorporated an *Ochromonas*-like constitutive mixotroph into the COBALT biogeochemical model, focusing on a 1-dimensional water column in the Sargasso Sea as a basis for inquiry. We found that light was the primary driver of acclimation, with a preference for photosynthesis in the euphotic zone and vice versa in the aphotic zone prior to mixing. A 3-fold increase in bacterivory resulting from mixotrophy accelerated the microbial loop, shifting biomass to higher trophic levels and increasing carbon export by more than 20%. Overall, our results demonstrate the importance of including mixotrophs in biogeochemical models for their important role in shaping food-web dynamics and the biological carbon pump. Though we found the effects of plasticity to be somewhat subtle in our 1D model, our methods provide a computational tractable way to implement phenotypic plasticity and optimization on a global scale. We expect future work to expand the domain and types of mixotrophy in ocean models and to explore stoichiometric synergies between dual metabolic strategies.

Plain Language Summary Mixotrophs are a class of plankton that both synthesize their own organic matter (via photosynthesis) and consume other organisms for nutrients. Mixotrophs have been experimentally shown to adjust their cellular contents to modulate investment into either strategy depending on which mode is more productive. Thus, we incorporated a phenotypically plastic mixotroph into a circulating ocean model that tracks biological and chemical composition. We focused on a mixotrophic genus of nanoplankton *Ochromonas* that primarily feeds on bacteria and limited our model domain to a single water column in the Sargasso Sea. Results showed light availability to be the primary factor in driving the mixotroph's acclimation, leading to a shift toward photosynthesis at shallow depths and grazing in deeper waters prior to ocean mixing effects. In addition, biomass was redistributed from bacteria and phytoplankton to plankton of higher trophic level while stimulating greater rates of carbon sinking into the deeper oceans. As climate change is expected to have an impact on the structure of plankton communities and nutrient distribution in the global oceans, incorporating mixotrophy into biogeochemical models is important for understanding how temperature shifts impact ecosystem and carbon dynamics.

1. Introduction

Mixotrophy, or metabolism that incorporates both autotrophic and heterotrophic pathways, is increasingly understood to be widespread in marine planktonic communities. With the ability to simultaneously photosynthesize and graze on prey, phagotrophic mixotrophs (sometimes termed "mixoplankton" (Flynn et al., 2019)) are theorized to have a large impact on ocean community structure and food web dynamics by facilitating the transfer of energy to higher trophic levels (Leles et al., 2018; Ward & Follows, 2016). Mixotrophic nanoflagellates are particularly important, as they comprise a sizable fraction of nanophytoplankton (Zubkov & Tarran, 2008) and contribute significantly to bacterial mortality in the marine food web (Hartmann et al., 2013). As a result, mixotrophs are also predicted to accelerate the biological pump in the process of redistributing carbon from the microbial loop into organisms with larger body sizes (Mitra et al., 2014; Ward & Follows, 2016).

Given their important role in shaping marine ecology and biogeochemistry, further modeling work that includes mixotrophy is vital for a complete picture of ocean ecosystems (Millette et al., 2023). Mixotrophs have previously been incorporated into regional ecosystem models that confirm their role in promoting trophic transfer efficiency and carbon cycling (Edwards, 2019; Leles et al., 2018, 2021; Mitra et al., 2014). To date, however, mixotrophs have been incorporated into few global Earth system models. One such model, the MIT-Darwin model, has incorporated mixotrophy, though limited to dinoflagellates with fixed nutritional modes (Archibald et al., 2022; Dutkiewic et al., 2020; Ward & Follows, 2016). As global ocean biogeochemical modeling is vital for tracking carbon and nutrient flow in light of climate change and fishery sustainability (Fennel et al., 2022; C. A. Stock et al., 2020), these models are incomplete without mixotrophy.

Furthermore, despite the fact that mixotrophs are known to vary their metabolic investment strategies, biogeochemical models that do include mixotrophs typically fix their metabolic strategies. For example, mixotrophic nanoflagellates have been empirically shown to adjust their relative investments in photosynthesis and grazing in response to environmental conditions, especially light availability and prey resource availability (Barbaglia et al., 2024; Lie et al., 2018; Wilken et al., 2020). Some smaller scale box models have simulated mixotroph plasticity by allowing metabolic strategy to converge on a maximum growth rate and found that variability in nutritional mode may alter mixotrophs' contributions to nutrient and carbon cycling (Archibald et al., 2024; Chu et al., 2023). A framework for plastic mixotrophy in large-scale biogeochemical modeling additionally allows for a spectrum of metabolic phenotypes that would traditionally be represented as separate functional groups (e.g., Ward & Follows, 2016) to be compressed into fewer tracers, saving computing time and costs. Nonetheless, mixotrophic plasticity has yet to be explored in a large-scale fully coupled biogeochemical setting.

To illustrate the effects of plastic mixotroph metabolic strategies on upper ocean ecosystem dynamics, we implemented a class of mixotrophic nanoflagellates into the Geophysical Fluid Dynamics Laboratory's (GFDL) model: Carbon, Ocean Biogeochemistry and Lower Trophics (COBALTv2) model, which simulates the interaction of phytoplankton, zooplankton, and bacteria with global biogeochemistry (C. A. Stock et al., 2020). We chose to model our mixotroph after the nanoflagellate *Ochromonas*, a widely distributed and well-studied genus of constitutive mixotrophs, which produce their own plastids as opposed to incorporating those of their prey (Mitra et al., 2016; Stoecker, 1998). *Ochromonas* is a prolific grazer on both bacteria (Lie et al., 2018; Wilken et al., 2020) and small eukaryotic phytoplankton (Moeller et al., 2019) with major implications for the microbial carbon loop (Andersson et al., 1989; Foster & Chrzanowski, 2012; Hartmann et al., 2013). We limited the model domain to the Bermuda Atlantic Time Series (BATS) location in the Sargasso Sea to focus on the dynamics of a plastic mixotroph in a one-dimensional vertical water column throughout the year. Mixotrophy is theorized to be advantageous in the surface waters of the Sargasso Sea where a dual metabolic pathway allows for efficient resource utilization in high-irradiance oligotrophic environments (Arenovski et al., 1995; Fischer et al., 2022; Moeller et al., 2024). Additionally, seasonal cycles of mixing and stratification at BATS induce variability in environmental conditions and resource availability (Longnecker et al., 2024; Viljoen et al., 2024), allowing us to assess how mixotrophs may vary their metabolic strategies in response. Coupling planktonic food web dynamics with full ocean model forcings through COBALT allows us to directly predict the consequences of mixotroph plasticity on community structure and nutrient distribution across the water column, with avenues to expand to other regions or the global ocean (Drenkard et al., 2025; Ross et al., 2023).

By incorporating mixotrophic nanoflagellates as a functional group into a fully coupled biogeochemical model at BATS, we address the following questions: (a) how does a mixotroph with dual metabolic modes persist in an oligotrophic environment, (b) what are the seasonal dynamics and optimal strategies of a metabolically plastic mixotroph, and (c) what are the ecological and biogeochemical impacts of introducing mixotrophs into a large-scale ocean model? This study aims to make predictions about trends in mixotrophy at scale, laying the foundations for a global implementation of constitutive mixotrophs in COBALT.

2. Methods

We implemented a one-dimensional column version of the Modular Ocean Model v6 (MOM6) (Adcroft et al., 2019) with the Carbon, Ocean Biogeochemistry, and Lower Trophics v2 (COBALTv2) model (C. A. Stock et al., 2020) in a 4×4 domain with 0.1° resolution at the Bermuda Atlantic Time Series (BATS) location (31.67°N, 64.17°W), collecting one-dimensional data as the horizontal average of the interior 2×2 grid. We used surface forcing from the Japanese 55-year Reanalysis (JRA55) (Kobayashi et al., 2015) with horizontal transport

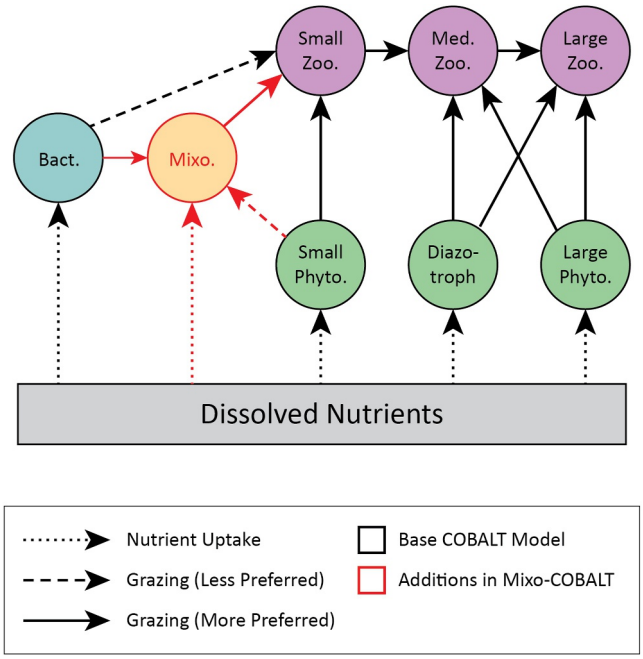

Figure 1. We integrated mixotrophic nanoflagellates into the COBALT food web, with new additions highlighted in red. The mixotrophs feed on bacterial and small phytoplankton, greatly preferring bacteria. In addition, the mixotroph is a potential prey source for small zooplankton, which prefer them equally to small phytoplankton.

subject to doubly periodic boundary conditions (Reichl & Hallberg, 2018). Additional sources of nutrients include atmospheric deposition of NH_4 and NO_3 (Horowitz et al., 2003), dust from Zhao et al. (2018) with soluble Fe calculated in accordance with Baker and Croot (2010). We initialized the model with outputs from a previous run of COBALT, consistent with C. A. Stock et al. (2020), incorporating an additional class of mixotrophs to the existing plankton functional groups with initial distribution identical to that of small phytoplankton. To account for unequilibrated model initialization, we ran the model with one year of spin-up followed by a second year where we collected daily averaged data, both years using the same 2004 environmental forcings.

The COBALTv2 model is fully described in previous publications C. A. Stock et al. (2014, 2020), so here we briefly summarize our modifications to relevant components of this model.

2.1. Implementation of Mixotrophy

The baseline COBALT model contains seven plankton functional types in total: three phytoplankton functional groups (small, large, and diazotroph), three zooplankton functional groups (small, medium, and large), and 1 bacterial group (for full details on the configuration of the baseline COBALTv2 food web, see C. A. Stock et al., 2014, 2020). The small and large phytoplankton functional types are roughly separated at an equivalent spherical diameter (ESD) of 10 μm, with small phytoplankton encompassing cyanobacteria and other small nanoflagellates, and the large phytoplankton functional type representing diatoms, coccolithophores, and other large phytoplankton. The diazotroph is modeled after *Trichodesmium*. The three zooplankton consume bacteria and phytoplankton, with the small zooplankton modeled as a microzooplankton (<200 μm ESD) that predates on small phytoplankton and partially predates on bacteria. The medium and large zooplankton are mesozooplankton (medium: 200–2,000 μm; large: 2–20 mm ESD).

As a starting point, we implemented the mixotroph by assigning it the photosynthetic capacity of a small phytoplankter and the phagotrophic capacity of a small zooplankter as already implemented in COBALT (Figure 1). To align our parameterization with the metabolism of *Ochromonas* (Figure 1), we increased the maximum heterotrophic ingestion rate at 0°C from the small zooplankton's 1.28 to 1.74 day^{-1}, based on an estimated value for *Ochromonas* of cell volume 200 μm^3 (Hansen et al., 1997).

The total flux of mixotroph biomass (M), incorporating per capita growth and respiration (μ_m) as well as loss fluxes (j), is given by

$$\frac{dM}{dt} = \underbrace{\mu_m(\eta,\psi)M}_{\text{Growth \& Respiration Terms}} \underbrace{- j_{graz} - j_{agg} - j_{vir} - j_{exu}}_{\text{Loss Terms}}. \quad (1)$$

As mixotrophy combines the respective metabolism of phytoplankton and zooplankton in the model, we express the per capita growth rate of the mixotrophs (μ_m) as a weighted sum of autotrophic growth (μ_a) and heterotrophic growth (μ_h). The relative contributions of these two modes are governed by two parameters: ψ and η.

$$\mu_m(\eta,\psi) = \mu_a(\eta,\psi) + \mu_h(\eta,\psi) \quad (2)$$

To capture the trade-off in investment between phototrophic and phagotrophic metabolism (Archibald et al., 2024; Chu et al., 2023; Moeller et al., 2024), the dimensionless parameter ψ (which takes a value between 0 and 1) represents the proportion of metabolic biomass invested into photosynthesis as opposed to grazing. Values closer to $\psi = 0$ indicate a greater investment into heterotrophy while values closer to $\psi = 1$ indicate a

greater investment into autotrophy. Respiration is also weighted by ψ as photosynthetic and phagotrophic cellular machinery may have different respiratory demands.

In addition, mixotrophic nanoflagellates appear to be less efficient at photosynthesis and phagotrophy than specialist competitors (Edwards et al., 2023), perhaps due to the resource costs of building and dismantling more cellular infrastructure (Litchman et al., 2007; Zubkov & Tarran, 2008). Thus, we use the dimensionless parameter η (which takes a value between 0 and 1) to account for the cost of metabolic generalism compared to specialization (Flynn & Mitra, 2009; Ward & Follows, 2016) as a flat penalization multiplier on growth rate. This means that our mixotroph cannot directly out-compete either phytoplankton or zooplankton functional group. Further, we found that the closer that η is to 0, the smaller the mixotroph abundance and the lower the mixotroph's impact on community composition (Figure S1 in Supporting Information S1). For our main results, we set $\eta = 0.9$ to represent a relatively efficient mixotroph.

The following sections provide further detail on the implementations of η and ψ for photosynthesis and grazing.

In accordance with other COBALT plankton tracers, we impose an internal stoichiometric ratio of 20N:1P on mixotrophs to align with small phytoplankton. Thus, nutrient uptake for photosynthesis is taken up according to this ratio whereas if N or P limits grazing, the excess nutrient is excreted as either phosphate or ammonium respectively. This allows the model to impose stoichiometric ratios while maintaining total nutrient amounts.

2.1.1. Autotrophic Growth

We define the mixotroph's autotrophic growth rate as the net difference between its photosynthetic growth and the portion of its metabolic respiratory costs to photosynthesis. Photosynthetic growth depends on temperature (T), nutrient limitation (N_{lim}), and instantaneous irradiance (I_{inst}) varying over the diel cycle using a modified version of the dynamic model of phytoplankton growth and acclimation described in Geider et al. (1997):

$$\mu_{\text{a}} = \frac{P_m^c}{1+\zeta}\left[1 - \exp\left(\frac{-\alpha I_{\text{inst}}\theta}{P_m^c}\right)\right] - \psi b_{\text{resp,a}} T_{\text{lim}}, \tag{3}$$

where P_m^c is the temperature-specific light-saturated photosynthetic rate, ζ is a biosynthetic cost, α is the chlorophyll-specific maximum initial slope of the Photosynthesis-Irradiance (PI) curve, θ is the chlorophyll to carbon ratio (Chl:C), and $b_{\text{resp,a}}$ is the autotrophic basal respiration rate. We scale the Chl:C ratio θ by ψ to account for differences in chlorophyll content across mixotrophs with different investment strategies (see below). We also multiply respiration by ψ to reflect the proportion of metabolic energetic costs due to phototrophy. Temperature limitation (T_{lim}) follows from Eppley (1972) using an exponential term with temperature constant k_T:

$$T_{\text{lim}} = \exp(k_T T). \tag{4}$$

Similarly, we scale the photosynthetic rate P_m^c with temperature and nutrient limitation, subject to the generalist penalization factor penalization η between 0 and 1:

$$P_m^c = \eta P_{\max}^c T_{\text{lim}} N_{\text{lim}}. \tag{5}$$

We determine nutrient limitation (N_{lim}) as the minimum of nitrate, ammonia, phosphate, and iron limitations using Liebig's Minimum Law (Liebig & Playfair, 1840).

$$N_{\text{lim}} = \min\left[(\text{NO}_3)_{\text{lim}}, (\text{NH}_4)_{\text{lim}}, (\text{PO}_4)_{\text{lim}}, \text{Fe}_{\text{lim}}\right] \tag{6}$$

Nitrate and ammonium limitation are calculated such that nitrate uptake is inhibited in the presence of ammonium and vice versa (O'Neill et al., 1989; C. A. Stock et al., 2014), with nitrate uptake much more inhibited by ammonia than the opposite (by roughly 50 times) as governed by the ratio of half-saturation parameters k_{NO_3} and k_{NH_4}:

$$(\text{NO}_3)_{\text{lim}} = \frac{\text{NO}_3}{k_{NO_3} + \text{NO}_3 + (k_{NO_3}/k_{NH_4})\,\text{NH}_4}, \tag{7}$$

$$(\mathrm{NH_4})_{\mathrm{lim}} = \frac{\mathrm{NH_4}}{k_{NH_4} + \mathrm{NH_4} + (k_{NH_4}/k_{NO_3})\,\mathrm{NO_3}}, \tag{8}$$

phosphate limitation is calculated using a saturating uptake function (Monod, 1949):

$$(\mathrm{PO_4})_{\mathrm{lim}} = \frac{\mathrm{PO_4}}{k_{PO_4} + \mathrm{PO_4}}, \tag{9}$$

and iron limitation follows a sigmoidal relationship with an internal cell quota, q_{Fe} defined as the ratio of internal iron to internal nitrogen biomass (Sunda & Huntsman, 1995):

$$\mathrm{Fe_{lim}} = \frac{q_{Fe}^2}{k_{Fe2N}^2 + q_{Fe}^2}. \tag{10}$$

The Chl:C ratio (θ) varies with irradiance using an irradiance memory term (I_{mem}) that lags behind instantaneous irradiance to account for photo-acclimation time. Additionally, the instantaneous irradiance term I_{mix} takes on the average irradiance of the mixed layer for depths in the mixed layer. In effect, I_{mem} captures the average light within a volume of water over roughly 24 hr to limit oscillations in the Chl:C ratio over the diel cycle. This is tracked in the model for each location and depth and is not affected by advection and diffusion, an approximation we address in the discussion section. The investment strategy (ψ) scales the mixotroph's minimum and maximum Chl:C ratio such that $\psi\theta_{\mathrm{min}} < \theta < \psi\theta_{\mathrm{max}}$:

$$\theta = \frac{\psi \times (\theta_{\mathrm{max}} - \theta_{\mathrm{min}})}{1 + (\psi\theta_{\mathrm{max}}\alpha I_{\mathrm{mem}})/\left(2P_m^c\right)} + \psi\theta_{\mathrm{min}}, \text{ where} \tag{11}$$

$$I_{\mathrm{mem}} = \int_0^{\infty} \gamma_I \exp\left(-\gamma_I \tau\right) I_{\mathrm{mix}}(t-\tau)\mathrm{d}\tau. \tag{12}$$

In this formulation, η and ψ affect the effective autotrophic growth rate in different ways: η reduces the total maximum growth rate of the mixotroph compared to a strict phytoplankter, while ψ reduces the Chl:C ratio through the production of fewer chloroplasts, decreasing the initial slope of the PI curve. In effect η induces a flat reduction in photosynthesis while ψ has the strongest effect in low-light conditions.

2.1.2. Heterotrophic Growth

We calculate the mixotroph's grazing growth rate similarly as the difference between ingestion and respiration:

$$\mu_{\mathrm{h}} = gge_{\mathrm{max}} I - (1-\psi) b_{\mathrm{resp,h}}, \tag{13}$$

where gge_{max} is the maximum gross growth efficiency of mixotroph grazing and $b_{\mathrm{resp},h}$ is the temperature-dependent basal respiration rate for grazing, which we have also scaled by the partial investment into heterotrophy given by $1 - \psi$. The mixotroph total ingestion rate (I) for n prey types

$$I = \eta \times (1-\psi) \times I_m \times \frac{\sum_{i=1}^{n} \mathrm{PA}_i p_i}{k_I + \sum_{i=1}^{n} \mathrm{PA}_i p_i}, \tag{14}$$

where each prey type i has biomass p_i and prey availability PA_i to the mixotroph, which we define below. In addition, η and $(1 - \psi)$ reduce the total ingestion rate to represent respectively the cost of generalism and the proportion of metabolism dedicated to predation. The temperature and oxygen-dependent grazing rate I_m is

$$I_m = I_{\mathrm{max}} T_{\mathrm{lim}} (\mathrm{O_2})_{\mathrm{lim}} \tag{15}$$

where T_{lim} follows Eppley temperature scaling from Equation 4 (Eppley, 1972), and the oxygen limitation $(\mathrm{O_2})_{\mathrm{lim}}$ is determined using a saturating uptake function with no ingestion in low-oxygen environments:

$$(O_2)_{\text{lim}} = \frac{\max(O_2 - O_{2,\min}, 0)}{k_{O_2} + \min(O_2 - O_{2,\min}, 0)} \tag{16}$$

Each prey type's availability to the mixotroph PA_i is calculated from an intrinsic preference for each prey type (innate prey availability) IPA_i:

$$PA_i = IPA_i \times \left(\frac{(IPA_i p_i)^2}{\sum_{j=1}^{n} (IPA_i p_i)^2} \right)^{1/2}, \tag{17}$$

which scales with the relative abundances of all prey types using a mild density-dependent switching behavior by the grazer. For the mixotroph, available prey types include bacteria ($IPA_{bact} = 1$) and small phytoplankton ($IPA_{smp} = 0.25$).

We modeled mixotroph grazing following existing zooplankton grazing functions in COBALT (C. A. Stock et al., 2014, 2020). Grazing functional forms have been investigated in COBALT in prior studies, including prey switching (C. Stock & Dunne, 2010; C. A. Stock et al., 2008); here we chose a Holling Type II functional form (Holling, 1966) and an ingestion matrix consistent with other grazers already parameterized in the model (C. A. Stock et al., 2020).

Egestion and excretion from grazing is partitioned by predefined fractions into detritus and dissolved nutrients as per Table 1.

2.1.3. Loss Terms

Mixotroph loss terms include grazing mortality, aggregation, viral lysis, and exudation.

Small zooplankton (smz) are able to graze on mixotrophs ($IPA_{mx} = 1$), who also graze on small phytoplankton ($IPA_{smp} = 1$) and bacteria ($IPA_{bact} = 0.25$) as shown in Figure 1. Small zooplankton grazing follows similar dynamics to Section 2.1.2 with parameterization identical to that of C. A. Stock et al. (2020). Thus, mixotrophs are subject to grazing mortality (j_{graz}) by.

$$j_{graz} = Z \times I_m \times \frac{PA_{mx} M}{k_I + \sum_{i=1}^{n} PA_i p_i} \tag{18}$$

where Z is the biomass of small zooplankton, M is the biomass of mixotrophs, and I_m and PA_i are calculated with the small zooplankton's parameters (C. A. Stock et al., 2020).

Aggregation loss (j_{agg}) follows quadratic density dependence such that aggregation is suppressed under high growth conditions and increases rapidly as growth drops below some fraction (f_{agg}) of the maximum possible growth rate at temperature T (Doney et al., 1996; Waite et al., 1992):

$$j_{agg} = (1 - \mu_{ratio})^2 m_{agg} M^2, \tag{19}$$

$$\mu_{ratio} = \min\left[\frac{\mu_{mem}}{f_{agg} P^c_{max} T_{lim}}, 1 \right], \tag{20}$$

$$\mu_{mem} = \int_0^{\infty} \gamma_\mu \exp(-\gamma_\mu \tau) \mu_a(t - \tau) d\tau, \tag{21}$$

where μ_{ratio} is the ratio of the mixotroph's time-averaged autotrophic growth memory (μ_{mem}) to some defined fraction (f_{agg}) of the maximum photosynthetic rate P^c_{max}, and m_{agg} is the aggregation rate constant. The autotrophic growth memory μ_{mem} is calculated as a time-average and tracked per location and depth similarly to the irradiance memory I_{mem}. The primary purpose of this is to dampen the effects of rapid changes in growth on aggregation loss due to the diel cycle or advection of plankton. All aggregated biomass is routed to the detrital pool.

Table 1
Mixotroph Photosynthesis, Grazing, and Loss Parametrization

Parameter	Name	Units	Value
k_T	Temperature scaling	$°C^{-1}$	0.063
$C2N$	C:N ratio	molC $molN^{-1}$	6.625:1
$P2N$	P:N ratio	molP $molN^{-1}$	1:20
Autotrophy parameters			
α	Chl-specific max init. slope of P-I curve	gC $gChl^{-1}$ m^{-2} J^{-1}	1.564e−4
$P^C_{\max}$	Maximum photosynthetic rate at 0°C	day^{-1}	1.25
ζ	Cost of biosynthesis	Dimensionless	0.05
$b_{\text{resp,a}}$	Basal autotrophic metabolic rate at 0°C	day^{-1}	0.03
$\theta_{\max}$	Maximum Chl:C ratio	gChl gC^{-1}	0.03
$\theta_{\min}$	Minimum Chl:C ratio	gChl gC^{-1}	0.002
γ_I	Irradiance memory decay rate	day^{-1}	1.0
k_{NH_4}	Half-saturation for ammonium limitation	µmol kg^{-1}	0.01
k_{NO_3}	Half-saturation for nitrate limitation	µmol kg^{-1}	0.5
k_{PO_4}	Half-saturation for phosphate limitation	µmol kg^{-1}	0.01
k_{Fed}	Half-saturation for dissolved iron uptake	µmol kg^{-1}	0.1
k_{Fe2N}	Half-saturation for iron cell quota limitation	nmol Fe mol N^{-1}	19.875
Heterotrophy parameters			
$I_{\max}$	Maximum ingestion rate at 0°C	day^{-1}	1.74[a]
k_I	Half-saturation for grazing	µmol N kg^{-1}	1.25
$b_{\text{resp,h}}$	Basal heterotrophic metabolic rate at 0°C	day^{-1}	0.025
$gge_{\max}$	Maximum gross growth efficiency	Dimensionless	0.4
IPA	Innate prey availability	Dimensionless	Bact.: 1[b] SP: 0.25[b]
k_{O_2}	Half-saturation for oxygen limitation	µmol kg^{-1}	8.0
$(O_2)_{\min}$	Minimum oxygen for grazing	µmol kg^{-1}	0.8
ϕ_{det}	Fraction of ingestion to detritus	Dimensionless	0.1
ϕ_{ldon}	Fraction of ingestion N to labile dissolved organic N	Dimensionless	0.14
ϕ_{sldon}	Fraction of ingestion N to semilabile dissolved organic N	Dimensionless	0.04
ϕ_{srdon}	Fraction of ingestion N to semirefractory dissolved organic N	Dimensionless	0.01
ϕ_{NH_4}	Fraction of ingestion N to ammonium	Dimensionless	0.3
ϕ_{ldop}	Fraction of ingestion P to labile dissolved organic P	Dimensionless	0.13
ϕ_{sldop}	Fraction of ingestion P to semilabile dissolved organic P	Dimensionless	0.04
ϕ_{srdop}	Fraction of ingestion P to semirefractory dissolved organic P	Dimensionless	0.03
ϕ_{PO_4}	Fraction of ingestion P to phosphate	Dimensionless	0.3
Loss parameters			
m_{agg}	Aggregation rate constant	day^{-1} µmol N^{-1} kg^{-1}	0.1
f_{agg}	Fraction of maximum growth to aggregation	Dimensionless	0.25
γ_μ	Growth memory decay rate	day^{-1}	1.0
m_{vir}	Viral lysis rate constant	day^{-1} µmol N^{-1} kg^{-1}	0.2
$\phi_{\text{vir,ldon}}$	Fraction of viral N to labile dissolved organic N	Dimensionless	0.7
$\phi_{\text{vir,sldon}}$	Fraction of viral N to semilabile dissolved organic N	Dimensionless	0.1
$\phi_{\text{vir,srdon}}$	Fraction of viral N to semirefractory dissolved organic N	Dimensionless	0.2

Table 1
Continued

Parameter	Name	Units	Value
$\phi_{vir,ldop}$	Fraction of viral P to labile dissolved organic P	Dimensionless	0.65
$\phi_{vir,sldop}$	Fraction of viral P to semilabile dissolved organic P	Dimensionless	0.15
$\phi_{vir,srdop}$	Fraction of viral P to semirefractory dissolved organic P	Dimensionless	0.2
f_{exu}	Fraction of NPP to exudation	Dimensionless	0.13

Note. All other values from small phytoplankton and zooplankton in C. A. Stock et al. (2020). [a]Hansen et al. (1997). [b]Lie et al. (2018), Wilken et al. (2020), and Moeller et al. (2019).

Mixotroph losses to viral lysis (j_{vir}) are modeled as quadratically density-dependent and temperature-dependent with rate constant (m_{vir}):

$$j_{vir} = T_{lim} m_{vir} M^2. \tag{22}$$

Viral losses are partitioned into the dissolved organic matter pools based on fixed ratios given in Table 1.

Finally, exudation loss (j_{exu}) is modeled as a constant fraction (f_{exu}) of phototrophic productivity,

$$j_{exu} = f_{exu} \mu_a M \tag{23}$$

with all exudation loss routed to labile dissolved organic matter.

2.1.4. Dynamic Metabolic Strategies

We aim to contrast mixotrophs with fixed metabolic strategies (constant ψ) and mixotrophs with dynamic metabolic strategies (variable ψ) in response to environmental conditions, consistent with experimental work on constitutive mixotrophs (Barbaglia et al., 2024; Wilken et al., 2020). To do this, we first interpret ψ as the photosynthetic fraction (i.e., plastid fraction) of mixotrophic metabolic biomass within each grid cell as opposed to the investment strategy of any individual mixotroph. This allows us to directly track the photosynthetic biomass M_a (initialized at half the total biomass $0.5M$) as an advected tracer (consistent with COBALT's approach to modeling tracer concentrations as opposed to planktonic agents) and calculate $\psi = M_a/M$ at the beginning of each timestep. This allows for the mixing of different investment strategies with circulation in the water column.

We allowed the mixotroph to change its metabolic strategy to maximize growth in its local environment. Growth and mortality $\left(\frac{dM}{dt}\right)$ are allotted to autotrophic biomass (M_a) and heterotrophic biomass (M_h) to maintain their existing proportions. At each time step, a constant fraction of M_a and M_h decays, and the mixotroph is presented with a binary decision to replenish this biomass with the production of either chloroplasts or digestive vacuoles. The mixotroph takes the choice that maximizes instantaneous growth rate by comparing the productivities of a strictly photosynthetic $(\mu_a^\star)$ and strictly phagotrophic mixotroph $(\mu_h^\star)$ as a proxy:

$$\mu_a^\star = \mu_a(\psi = 1) \qquad \text{(where } I_{mem} \text{ is replaced with } I_{inst}\text{)}, \tag{24}$$

$$\mu_h^\star = \mu_h(\psi = 0). \tag{25}$$

Under conditions in which complete phototrophy would be more productive $(\mu_a^\star > \mu_h^\star)$, the value of ψ shifts toward 1, and vice versa. For the hypothetical strict phototroph, instead of using the 24-hr average irradiance I_{mem} in the calculation of the Chl:C ratio as in Equations 11 and 12, we substitute it with I_{inst}, which responds instantaneously to the diel light cycle. Assuming an asymptotic rate of approach ν, we use the following differential equations to describe this process:

$$\frac{dM_a}{dt} = \begin{cases} \frac{M_a}{M_a + M_h}\left(\frac{dM}{dt}\right) + \nu M_h & \mu_a^\star > \mu_h^\star \\ \frac{M_a}{M_a + M_h}\left(\frac{dM}{dt}\right) - \nu M_a & \mu_a^\star < \mu_h^\star, \\ \frac{M_a}{M_a + M_h}\left(\frac{dM}{dt}\right) & \mu_a^\star = \mu_h^\star \end{cases} \tag{26}$$

$$\frac{dM_h}{dt} = \begin{cases} \frac{M_h}{M_a + M_h}\left(\frac{dM}{dt}\right) - \nu M_h & \mu_a^\star > \mu_h^\star \\ \frac{M_h}{M_a + M_h}\left(\frac{dM}{dt}\right) + \nu M_a & \mu_a^\star < \mu_h^\star. \\ \frac{M_h}{M_a + M_h}\left(\frac{dM}{dt}\right) & \mu_a^\star = \mu_h^\star \end{cases} \tag{27}$$

In terms of ψ (represented by $M_a/(M_a + M_h)$), this reduces to

$$\frac{d\psi}{dt} = \begin{cases} \nu(1-\psi) & \mu_a^\star > \mu_h^\star \\ -\nu\psi & \mu_a^\star < \mu_h^\star. \\ 0 & \mu_a^\star = \mu_h^\star. \end{cases} \tag{28}$$

The parameter ν sets a maximum rate of change for ψ, with 0 indicating a completely static strategy and larger values corresponding to faster rates of phenotypic acclimation. We take $\nu = 1.0\ \text{day}^{-1}$ to match the exponential kernel decay rates of irradiance memory (γ_I) and growth memory (γ_μ), but see Results below and Figure S3 in Supporting Information S1 for the effects of other ν values.

We modeled phenotypic plasticity this way as opposed to an evolutionary model because, in our view, this approach more faithfully represents a reasonable mechanism by which the mixotroph can measure and adjust resource acquisition and utilization of its plastids on a short time scale. That is, we envision that a mixotroph can compare the relative performance of a chloroplast and a digestive vacuole inside of its cell, and choose which structure to build next on this basis. However, we acknowledge that the use of a fitness gradient could produce different results, which we do not explore here.

For a full list of mixotroph parameters, refer to Table 1.

2.2. Model Validation

For model validation, we ran two models: a static mixotroph with investment into phototrophy and phagotrophy ($\eta = 0.9, \psi = 0.5, \nu = 0$) and a model absent of mixotrophs ($\eta = 0$), comparing both models with observational data from the BATS station (Figure 2, Table 2).

The one-dimensional version of COBALT aligns well with predictions of NPP, but varies in consistency with nitrate and phosphate concentrations, even in the absence of mixotrophy (Figure 2). Predictions of NPP worsen with the introduction of a static mixotroph, though nitrate and phosphate estimations improve (Table 2). It is important to note that since COBALT is primarily a global model, it may not necessarily resolve specific sites especially precisely.

2.3. Sensitivity Analysis

We performed three sensitivity tests on the mixotroph to assess the role of light, nutrient, and prey availability on our mixotroph's investment strategy, each of which affect productivity with a saturating response curve. We modulated the initial slope of each of these response curves by either 50% or 200% through α for light availability (Equations 3 and 11), nutrient limitation half-saturation constants $(1/k_{NO_3}, 1/k_{NH_4}, 1/k_{PO_4}, 1/k_{Fe})$ for nutrient

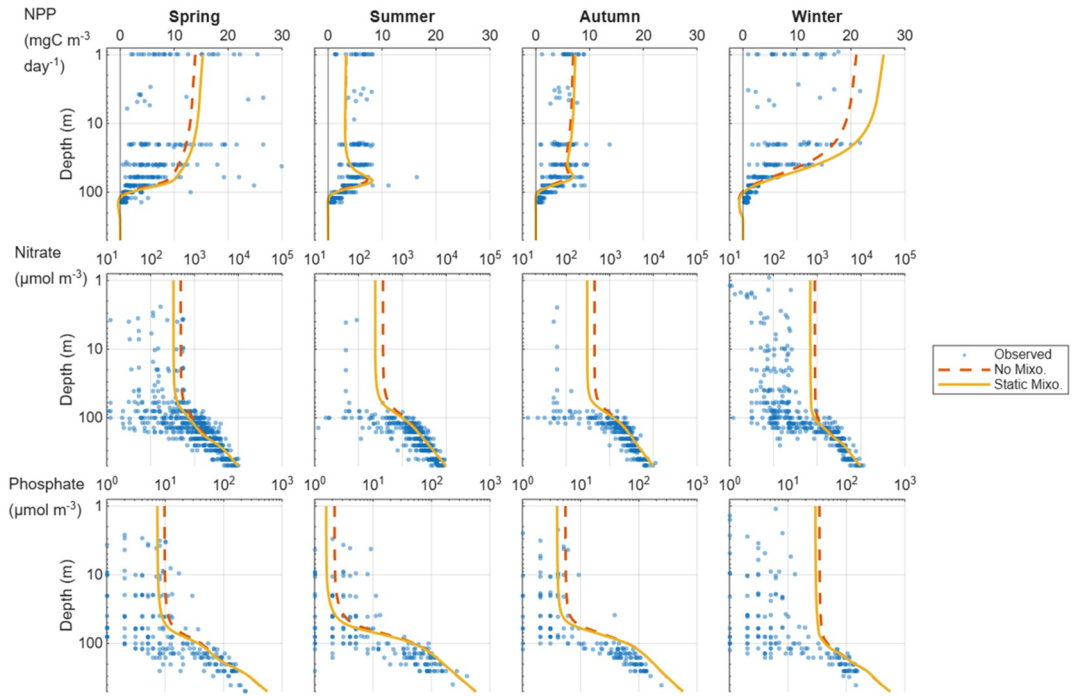

Figure 2. Model outputs including a static mixotroph (solid line) as well as one without mixotrophy (dashed line) were compared against discrete bottle samples at BATS in the top 150 m from 2000 to 2009 (inclusive). Soluble Reactive Phosphorus (SRP) data was used for bioavailable phosphorus validation. We time-averaged model outputs over each season and plotted depth and nutrient concentrations on a log scale.

availability (Equations 6–10), and prey availability (Equation 14), after which the average biomass-weighted investment strategy ψ was measured. Results are discussed in Section 3.2 and Figure 6.

3. Results

3.1. Persistence of Mixotrophic Nanoflagellates in an Oligotrophic Gyre

We first characterized the persistence of a mixotrophic nanoflagellate in the Sargasso Sea by considering a static metabolic strategy that equally weights photosynthetic and grazing investments ($\eta = 0.9$, $\psi = 0.5$, $\nu = 0$). The model captured typical seasonal physical oceanography in the Sargasso Sea, with annual variation in the depth of well-homogenized surface water (a.k.a., "mixed layer") that regulates the biomass and productivity of plankton (Figure S2 in Supporting Information S1). Dividing the year into four seasons (Spring = March–May, Summer = June–August, Autumn = September–November, and Winter = December–February), a deep mixed layer depth (MLD) led to upwelling of sunken nutrients in winter and spring, stimulating homogeneously high biomass and productivity throughout the mixed layer (Figures 3a, 3d, 3e, and 3h). During summer shoaling of the mixed layer, the surface waters became oligotrophic in the stratified ocean, reducing total productivity and biomass (Figures 3b, 3c, 3f, and 3g).

Additionally, a shallow summer mixed layer led to the formation of a deep chlorophyll maximum (DCM; Figure S2 in Supporting Information S1). Similarly to small phytoplankton, the static mixotroph's biomass peaked in the DCM during summer and autumn (Figures 3b, 3c, 3f, and 3g). Therefore, we defined the DCM region as 60–100 m deep, contrasting community composition and function between the DCM with the variable surface mixed layer for subsequent analyses (Figure S2 in Supporting Information S1). We recognize that this is shallower than the typical 100 m DCM observed at

Table 2
Error Metrics in the Top 100 m for the Default 1D COBALT (NM = No Mixotroph) and Mixo-COBALT (SM = Static Mixotroph) Compared to Empirical Data From BATS From 2000 to 2009 Inclusive: Linear Correlation, Bias, and Root Mean Square Error

		Correlation		Bias		RMSE	
Tracer	# Obs.	NM	SM	NM	SM	NM	SM
NPP (mg C m^{-3} day^{-1})	762	0.609	0.593	2.13	3.28	5.85	7.36
Nitrate (μmol m^{-3})	1,510	0.327	0.328	583	425	651	509
Phosphate (μmol m^{-3})	427	0.281	0.293	14.0	11.3	22.2	19.6

Note. Soluble Reactive Phosphorus (SRP) data was used for bioavailable phosphorus validation. Model predictions for observed data were calculated using a 1 month moving average and linearly interpolating between depth bins in the model output.

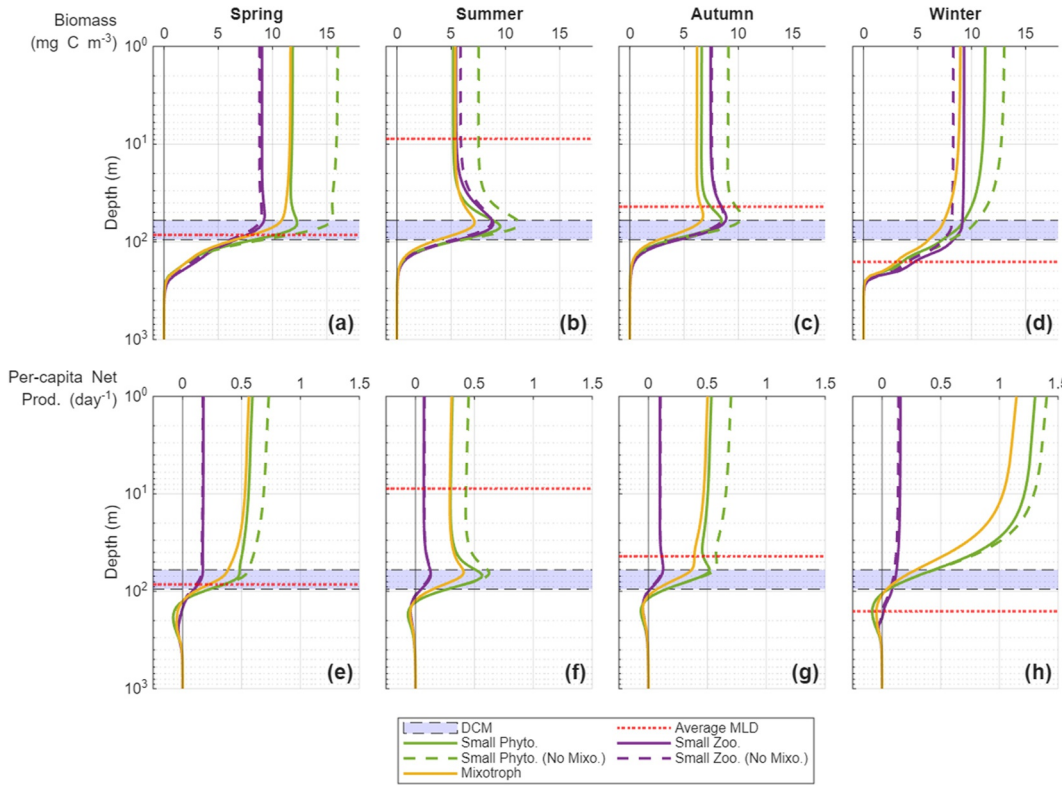

Figure 3. (a–d) Biomass and (e–h) per capita productivity of the mixotroph, small phytoplankton, and small zooplankton were separated by season and plotted against depth. Phytoplankton and zooplankton performance absent of mixotrophy were also included as a dashed line for comparison. We note variation in the mixed layer depth (MLD; the seasonal average marked as a red dashed line) as well as spikes in the deep chlorophyll maximum region (DCM; marked in light blue; Figure S2 in Supporting Information S1) observed in the summer.

BATS (e.g., Casey et al., 2007), which is a known bias within COBALTv2 (Moeller et al., 2019; C. A. Stock et al., 2020), though this should not qualitatively impact the relative tradeoff between dynamic and static mixotrophy central to our analysis.

Overall, we found that the mixotroph persisted in the ecosystem throughout the year, with biomass and productivity patterns that mirrored small phytoplankton (Figure 3). Interestingly, the discrepancy in productivity between small phytoplankton and mixotrophs was greatest under high-nutrient conditions such as at the winter surface or summer DCM, where phytoplankton more successfully outcompeted mixotrophs (Figures 3e, 3f, 3g,

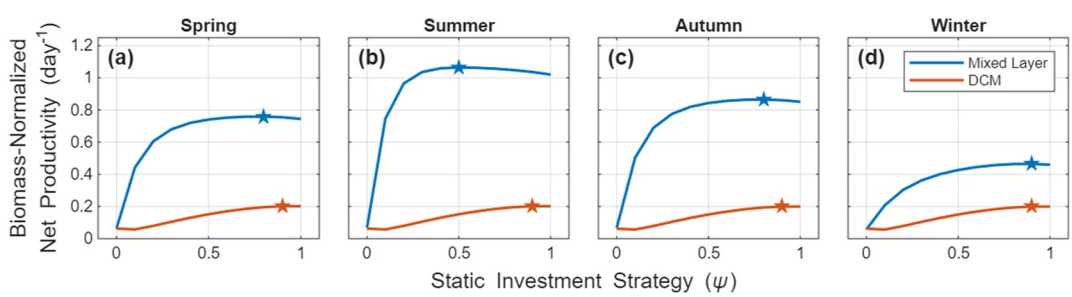

Figure 4. We plotted the mixotroph's per capita productivity across a range of fixed metabolic strategies, comparing across seasons (a–d) as well as between the surface mixed layer (blue line) and DCM region (orange line). Stars mark the growth-maximizing strategy for its respective depth bin and season. Per-capita productivity was calculated first as a vertical integral and subsequently time-averaged.

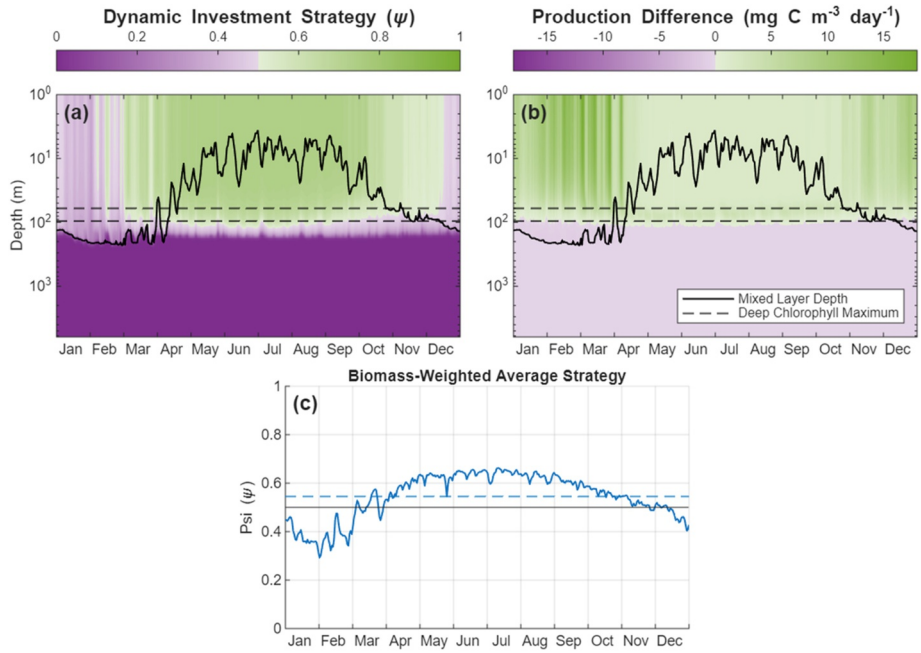

Figure 5. Panel (a) shows the dynamically varying investment strategy of the mixotroph with maximum acclimation rate maximum rate $\nu = 1.0\ \text{day}^{-1}$. Panel (b) plots the difference in production between a completely phototrophic and phagotrophic mixotroph, which is responsible for the mixotroph's direction of dynamic acclimation (Equations 24, 25, and 28). We averaged the investment strategy across depth and weighting by biomass to obtain panel (c), with an overall annual average of $\psi = 0.545$ marked as a dashed line.

and 3h). This suggests that mixotrophic generalism was most competitively viable under oligotrophic conditions, though small phytoplankton were never competitively excluded.

3.2. Differences in Optimal Growth Strategies Between Static and Dynamic Mixotroph

To account for mixotrophs' variable metabolic investment into photosynthesis and grazing, we tested a variety of fixed ψ values (i.e., $\nu = 0$) and found that throughout the year, per capita productivity was lowest with exclusive heterotrophy ($\psi = 0$) and increased to a plateau as the metabolic mode shifted toward autotrophy (Figure 4). Across seasons and depth bins, the optimal growth-maximizing strategy remained predominantly autotrophic (i.e., $\psi > 0.75$) except in the oligotrophic summer mixed layer, where an intermediate strategy ($\psi = 0.5$) was slightly more productive (Figure 4).

When we instead allowed the mixotroph to vary its investments as described in Equation 28 with a maximum rate of $\nu = 1.0\ \text{day}^{-1}$, the mixotrophs converged on a homogeneous strategy by depth within the mixed layer, with the ψ value corresponding closely with the MLD. Heterotrophy was preferred within the winter deep mixed layer in winter and autotrophy in the shallow summer mixed layer, though the average ψ value of did not differ drastically from a 50:50 split (Figures 5a and 5c). With the current parameterization, mixing acted on a faster time scale than the mixotrophs could change their strategy, leading to homogeneity of ψ in the mixed layer; however, varying the speed of mixotrophic acclimation (ν) modulated the relative impact of mixing on metabolic strategy but the average ψ value remained relatively consistent (Figure S3 in Supporting Information S1). We observed throughout the year that the mixotroph became more autotrophic above 100 m and heterotrophic below 100 m as demonstrated by the relative difference in productivity between phototrophic and phagotrophic strategies that guides acclimation (Figure 5b). This suggests that the deeper mixed layer injected heterotrophic mixotroph biomass into shallower waters in winter, decreasing the average ψ value, but summer stratification preserved a photosynthetic preference in the mixed layer. Notably, these results deviate from the expected trends in Figure 4, where the ability to alternate to a heterotrophic mode was preferred in summer as opposed to winter.

The causal mechanism behind the dynamic mixotroph's growth-maximizing ψ investment strategy was primarily light availability. Comparing against mixotrophs with altered response to irradiance, nutrients, and prey reveals

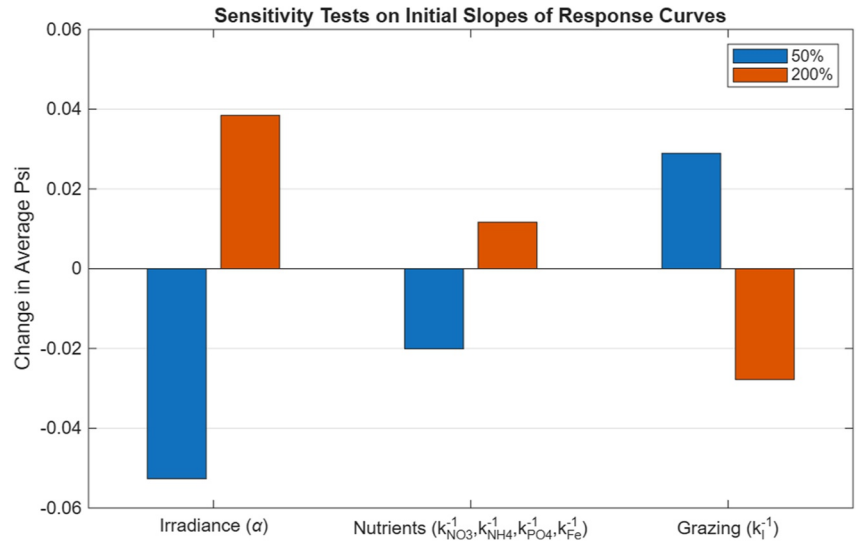

Figure 6. We compared our standard model to models with altered mixotroph parameterization to assess the role of various factors on mixotroph investment strategies. Namely, we halved and doubled the initial slopes of the mixotroph's response curves to irradiance (α), nutrient concentrations ($1/k_{NO_3}, 1/k_{NH_4}, 1/k_{PO_4}, 1/k_{Fe}$), and prey availability ($1/k_I$), and measured the resulting change in the average investment strategy. Average ψ was measured with a biomass weighted average across the water column and subsequently time-averaged.

that their investment strategy was most greatly influenced by changes in sensitivity to light, followed by prey and lastly nutrients (Figure 6). This is consistent with our observation that the direction of phenotypic acclimation was entirely stratified by depth (Figure 5b) where we would expect tracers such as nutrient and prey availability to follow the advection dynamics of the MLD. Combined with the sensitivity of the effect of ψ to light, this leaves irradiance as a primary candidate for driving the mixotroph's metabolic strategy in the Sargasso Sea.

3.3. Carbon Redistribution Due To Elevated Productivity and Displacement of Phytoplankton and Bacteria

We assessed the ecological impact of the mixotroph by comparing simulations with no mixotroph, a static mixotroph ($\psi = 0.5$, $\nu = 0\,\mathrm{day}^{-1}$), and a dynamic mixotroph (ψ variable, $\nu = 1.0\,\mathrm{day}^{-1}$) and found that mixotrophy broadly redistributed the biomass of lower trophic levels to higher trophic levels, though the total planktonic biomass changed by less that 1% in both cases. The introduction of a bacterivorous nanoflagellate led to an expected reduction in bacterial biomass due to grazing, while phytoplankton similarly decreased as a result of competition for photosynthetic resources and grazing pressure on small phytoplankton (Figure 7). Small to medium-size zooplankton marginally increased with the introduction of a new mixotrophic prey source to support higher trophic levels; however, large zooplankton decreased, seemingly because declines in large phytoplankton prey were not sufficiently compensated for by increases in medium zooplankton prey (Figure 7). The community structure did not differ greatly between a static and dynamic mixotroph (Figure 7). We did not observe strong seasonality in the mixotroph's impacts on bacteria, though the marginal impact on small phytoplankton biomass was largest in the oligotrophic summer and autumn, reflecting greater nutrient competition, while the marginal positive impact on small to medium-sized zooplankton was largest in winter, reflecting greater surges in prey biomass density (Figure S4 in Supporting Information S1).

Consistent with existing predictions (e.g., Stoecker et al., 2017; Ward & Follows, 2016), the changes to carbon flow reveal that mixotrophs drove higher productivity and increased the rate of carbon sequestration. Despite lowered bacterial biomass from increased bacterivory (Figures 7 and 8a), total bacterial productivity and net primary productivity actually increased (Figures 8b and 8c), indicating an increase in turnover rates. While the total DOC flux remained unchanged, sources of DOC shifted from density-dependent factors (i.e., viral lysis) to production-dependent factors (i.e., exudation and grazing egestion), which on average produced more refractory dissolved organic matter (Figure 8e, (C. A. Stock et al., 2020)). As a result, carbon export at 100 m substantially increased by about 20% (Figure 8d). A breakdown of export production showed that the increase observed here

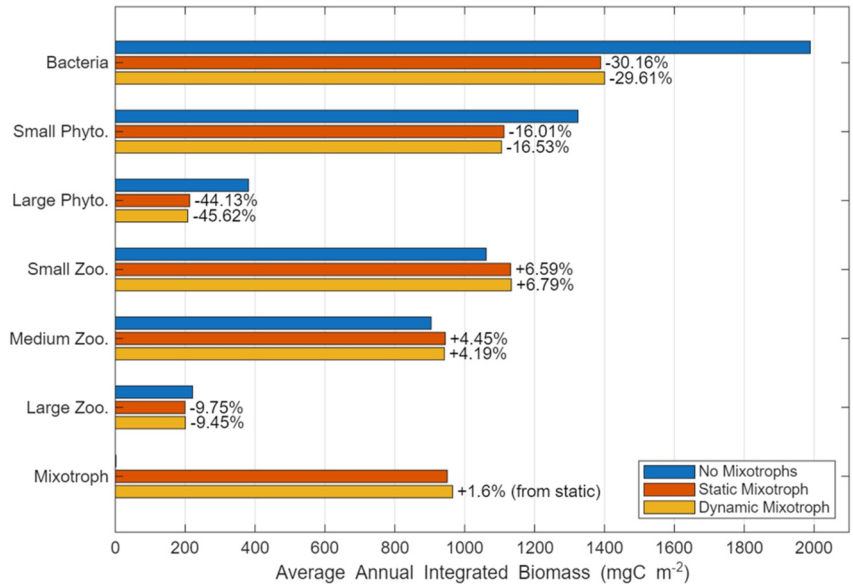

Figure 7. The change in biomass of various plankton functional groups with the introduction of either a static or dynamic mixotroph is shown. Biomass was integrated across the entire water column with an annual time average.

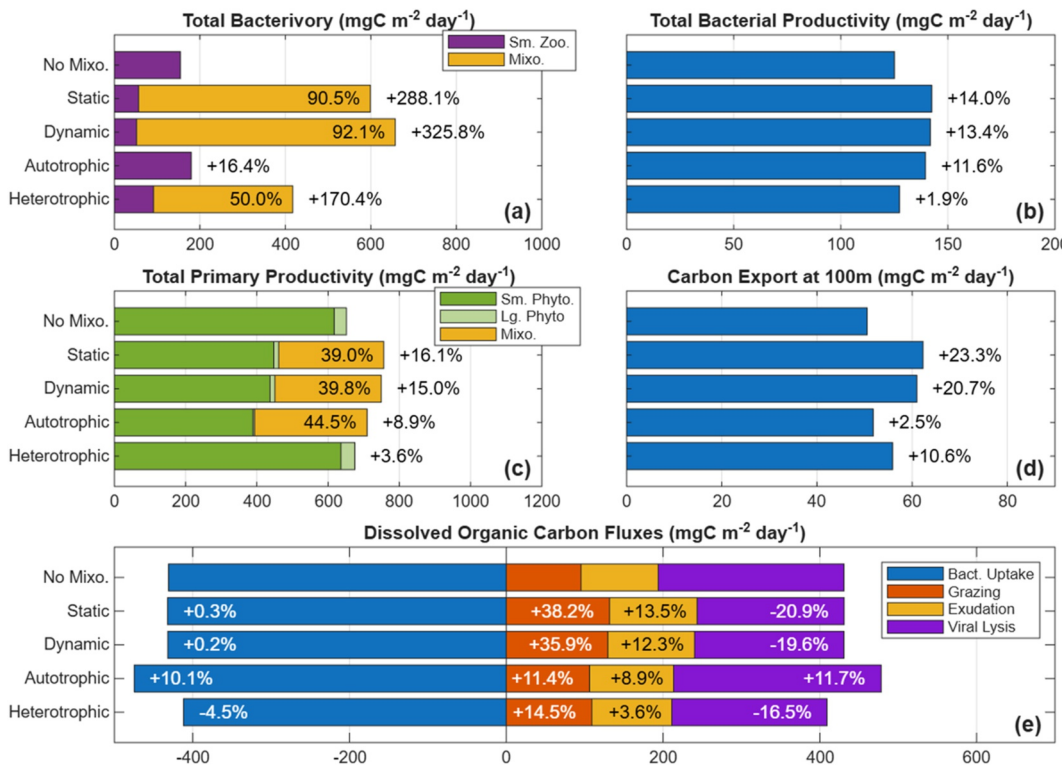

Figure 8. The bars of each chart represent models with (1) no mixotrophs; (2) a static mixotroph with $\psi = 0.5, \eta = 0.9$; (3) a dynamic mixotroph with $\nu = 1.0$ days$^{-1}, \eta = 0.9$; (4) an equivalently size-classed strict autotroph $\psi = 1.0, \eta = 1.0$; and (5) an equivalently size-classed strict heterotroph $\psi = 0.0, \eta = 1.0$ panels (a–c) show increases in bacterivory, bacterial productivity, and primary productivity respectively with the introduction of either mixotroph. The resultant increase in carbon export at 100 m is shown in panel (d). Panel (e) breaks down the changes in the sources dissolved carbon fluxes. Overall trends in carbon fluxes show that the introduction of mixotrophs largely increases productivity and turnover rates.

was largely accounted for by elevated grazing activity while decreases in the contributions by phytoplankton via aggregation were balanced by mixotroph aggregation (Figure S4 in Supporting Information S1).

This raises the question of whether the biogeochemical changes we observed were in fact due to mixotrophic metabolism or simply the result of introducing an additional functional type at this size class with a distinct ecological niche. Comparing against equivalent strict autotrophs and heterotrophs, we found that including a dynamic mixotroph elevated bacterivory, bacterial production, primary production, equally or more than either equivalent autotroph or heterotroph (Figures 8a–8c). Combining the increased primary production from autotrophy and increased export efficiency from heterotrophy allows for mixotrophy to induce an even greater overall increase in carbon export (Figure 8d).

We did not find major differences in environmental impact between a static and dynamic mixotrophs, though increased bacterivory by mixotrophs had marginal effects on biogeochemical cycling. Given that the average ψ value did not deviate especially far from 0.5 (Figure 5c), we did not observe a large difference the annually averaged biomass of any individual plankton group between models of static and dynamic mixotrophy (Figure 7 and Figure S5 in Supporting Information S1). However, dynamic strategy acclimation led to a 20.0% increase in mixotrophic bacterivory compared to a static mixotroph, while their effect on carbon export was reduced by 11.2% (Figure 8). The export ratio, defined as the fraction of NPP contributing to carbon export, increased from 7.76% to 8.23% with a static mixotroph while the dynamic mixotroph elevated it slightly less to 8.14%.

4. Discussion

Oceanographers have long posited that, because of their dual role as primary producers and grazers, mixotrophs may serve as "short circuits" in the planktonic food web, allowing rapid recycling of nutrients into photosynthetic biomass (Mitra et al., 2014; Moeller et al., 2024; Stoecker, 1998). Our results align with existing predictions that mixotrophic protists promote productivity despite decreased biomass, suggesting increased turnover and ultimately driving excess dissolved nutrients toward sequestration (Mitra et al., 2014; Ward & Follows, 2016). Thus, we emphasize the importance of incorporating mixotrophic nanoplankton into biogeochemical models for their major ramifications in estimates of carbon sequestration, especially in light of climate trends (Jassey et al., 2015; Puglia et al., 2026) which may alter mixotrophs' relative investments in photosynthesis and grazing (Lepori-Bui et al., 2022; Princiotta et al., 2016; Wilken et al., 2013). However, caution must be taken to avoid over-extrapolating the present results to the global ocean as incorporating ecosystem components large-scale constraints in a global model may lead to redistribute export as opposed to a net increase (Luo et al., 2022).

We found that the inclusion of mixotrophic nanoflagellates additionally altered community composition by shifting the distribution of biomass to higher trophic levels and reducing bacteria and phytoplankton through grazing and competitive displacement. The high irradiance and oligotrophic conditions typical of BATS may allow for mixotrophs to effectively compete with phytoplankton despite the penalized mixotroph productivity relative to that of specialist phytoplankton and zooplankton (Crane & Grover, 2010; Edwards, 2019). At the same time, substantial mixotrophic bacterivory has been shown to play a key role in regulating food web function in Atlantic oligotrophic gyres (Hartmann et al., 2012, 2013), allowing for mixotrophs and microzooplankton in our model to coexist through partitioning grazing niches between bacteria and phytoplankton respectively. Mixotrophic protists led to an average overall increase in cell size as grazing restricts the biomass of small plankton in favor of higher trophic levels, consistent with previous global modeling work that also found that mixotrophs enhanced carbon export (Ward & Follows, 2016).

As one of the first coupled biogeochemical models to include dynamic mixotrophy, our results provide insight into the behavior and environmental effects of a mixotroph that varies its metabolic investments. Pragmatically, our formulation allowed us to capture a wide array of mixotroph metabolic investment strategies with a single, temporally and spatially varying, mixotroph type, balancing computational efficiency with biological realism (Le Quéré et al., 2005). As we found dynamic mixotrophy to elevate carbon export less than static strategies (Figure 8), our model suggests a potential connection between mixotroph plasticity and biogeochemical cycling. Previous studies have shown that grazing activity has a greater tendency than photosynthesis to release recalcitrant carbon that is more subject to sequestration (Hessen et al., 2004; Tranvik, 1994), some drawing connections between mixotroph metabolism and carbon cycling (Archibald et al., 2024; Wilken et al., 2014). These

results warrant further investigation into the extent to which mixotrophs' seasonal cycling of nutritional modes affects biogeochemical processes.

Investigating the patterns of metabolic strategy themselves, our dynamic mixotroph skewed heterotrophic during winter and spring blooms and autotrophic during summer and autumn oligotrophy, demonstrating inconsistent agreement with existing predictions about mixotrophs in the Sargasso Sea. Under oligotrophic summer conditions, mixotrophs are expected to invest heavily in phagotrophy to support nitrogen acquisition and compete with specialist phytoplankton (Arenovski et al., 1995; Chu et al., 2023; Moeller et al., 2024) while dissolved nutrient availability during spring blooms favor autotrophy (Archibald et al., 2024). On the other hand, other studies have found that mixotrophs are most effectively able to compete with specialist zooplankton in largely low-irradiance high-nutrient environments that may not reflect the surface oceans of the Sargasso Sea (Edwards, 2019; Princiotta et al., 2023). Our mixotroph tended toward a "default" autotrophic mode where light is available, only turning toward phagotrophy to supplement nutritional needs in low light as some models have suggested (Crane & Grover, 2010). It is important to note that our study is limited to one site and that running global simulations in COBALT, as it is primarily tuned to do, may yield differing results.

Alternative formulations of mixotrophy may also alter this prediction. For example, allowing mixotrophs to sample over the entire ψ space (rather than making a binary comparison between phototrophy and phagotrophy; Equation 28) could produce distinct growth-maximizing strategies (Archibald et al., 2024), though this could be computationally intractable. Further, we accounted for the effects of photosynthetic investment by incorporating ψ into our equation for θ, the chlorophyll to carbon ratio of the mixotroph. While we made this choice to directly mimic the biological effects of investment (i.e., mixotrophs with higher photosynthetic investment would have higher chlorophyll content), the light-saturating photosynthesis-irradiance curve in COBALT is most sensitive to θ at low light levels (C. A. Stock et al., 2014). Thus, the effects of ψ were stronger at depth compared to the well-lit surface (Figure S6 in Supporting Information S1), contributing to the abrupt, depth-dependent shift in mixotroph optimal ψ values observed in our results. The preference for photosynthetic tendencies could also be reduced by tuning the model to more precisely reflect empirical data such as by adjusting cell size dynamics to align with empirical data on mixotrophy (Våge et al., 2013).

Moreover, generalist mixotroph strategies have been theorized to be advantageous in low-nutrient environments (Faure et al., 2019; Leles et al., 2017; Ward et al., 2011) because nutrients acquired via grazing may support sustained mixotroph photosynthesis (Flynn & Mitra, 2009; Ward et al., 2011). However, the COBALT model is not a quota model, and therefore does not allow for this synergy between forms of metabolism. (i.e., in our formulation, mixotrophs cannot, e.g., combine extra nitrogen from grazing and carbon from photosynthesis to produce new biomass. Rather, our model assumes strictly additive contributions of phototrophy and phagotrophy to growth, doubly excreting excess nutrients in the process.) Additionally, COBALT's formulation with population-level Monod kinetics as opposed to an agent-based quota model may lead to some error, particularly where mixing populations are heterogeneous (Baudry et al., 2018; Hellweger & Kianirad, 2007). For instance, a lack of internal quota or life history modeling results in a calculation of Chl:C ratio (Equations 11 and 12) that is best approximated for the well-homogenized mixed layer. Future work in upper ocean biogeochemical models could use quota-based or similar approaches that allow for synergies between metabolic modes as well as tracking of life history (Mitra et al., 2016; Moeller et al., 2024; Ward et al., 2011; Wilken et al., 2014).

Regardless of investment formulation, however, our model consistently predicts that mixotrophs amplify biogeochemical processes. Therefore, we argue that due to their ramifications for the biological pump, community structure, and food web energetics, mixotrophy is a vital component to consider in biogeochemical modeling. Though we observed marginal aggregate effects of a dynamic mixotrophy at BATS, seasonal and depth-based variability in strategy may have more pronounced impacts on carbon cycling and trophic dynamics in more variable coastal systems that should not be ignored. We hope that future work continues to recognize and explore mechanisms of plasticity in mixotrophs and expand the functional scope of mixotrophy in modeling.

Conflict of Interest

The authors declare no conflicts of interest relevant to this study.

Availability Statement

Model code and initialization are available at Sheu (2026a). Model output and MATLAB code for generating figures are also available at Sheu (2026b). Data from the Bermuda Atlantic Time Series (BATS) Hydrostation is available at Johnson et al. (2026).

Acknowledgments
We would like to thank Charles Stock and Niki Zadeh from the Geophysical Fluid Dynamics Laboratory for their help on the creation and one-dimensional implementation of COBALTv2. We would also like to thank Charlotte Laufkötter and Lana Flanjak from Bern University for their advice on biogeochemical analysis. This work was supported by the National Science Foundation (Grant OCE-2237017 to H.V.M.) and the Simons Foundation Postdoctoral Fellowship in Marine Microbial Ecology (award 990798 to K.M.A.).

References

Adcroft, A., Anderson, W., Balaji, V., Blanton, C., Bushuk, M., Dufour, C. O., et al. (2019). The GFDL global ocean and sea ice model OM4.0: Model description and simulation features. *Journal of Advances in Modeling Earth Systems*, *11*(10), 3167–3211. https://doi.org/10.1029/2019ms001726

Andersson, A., Falk, S., Samuelsson, G., & Hagström, Å. (1989). Nutritional characteristics of a mixotrophic nanoflagellate, *Ochromonas* sp. *Microbial Ecology*, *17*(3), 251–262. https://doi.org/10.1007/bf02012838

Archibald, K. M., Dutkiewicz, S., Laufkötter, C., & Moeller, H. V. (2022). Thermal responses in global marine planktonic food webs are mediated by temperature effects on metabolism. *Journal of Geophysical Research: Oceans*, *127*(12), e2022JC018932. https://doi.org/10.1029/2022jc018932

Archibald, K. M., Dutkiewicz, S., Laufkötter, C., & Moeller, H. V. (2024). Emergent trade-offs among plasticity strategies in mixotrophs. *Journal of Theoretical Biology*, *590*(6), 1557–1569. https://doi.org/10.1016/j.jtbi.2024.111854

Arenovski, A. L., Lim, E. L., & Caron, D. A. (1995). Mixotrophic nanoplankton in oligotrophic surface waters of the Sargasso Sea may employ phagotrophy to obtain major nutrients. *Journal of Plankton Research*, *17*(4), 801–820. https://doi.org/10.1093/plankt/17.4.801

Baker, A. R., & Croot, P. L. (2010). Atmospheric and marine controls on aerosol iron solubility in seawater. *Marine Chemistry*, *120*(1–4), 4–13. https://doi.org/10.1016/j.marchem.2008.09.003

Barbaglia, G. S., Paight, C., Honig, M., Johnson, M. D., Marczak, R., Lepori-Bui, M., & Moeller, H. V. (2024). Environment-dependent metabolic investments in the mixotrophic chrysophyte *Ochromonas*. *Journal of Phycology*, *60*(1), 170–184. https://doi.org/10.1111/jpy.13418

Baudry, J., Dumont, D., & Schloss, I. (2018). Turbulent mixing and phytoplankton life history: A Lagrangian versus Eulerian model comparison. *Marine Ecology Progress Series*, *600*, 55–70. https://doi.org/10.3354/meps12634

Casey, J. R., Lomas, M. W., Mandecki, J., & Walker, D. E. (2007). *Prochlorococcus* contributes to new production in the Sargasso Sea deep chlorophyll maximum. *Geophysical Research Letters*, *34*(10), L10604. https://doi.org/10.1029/2006gl028725

Chu, T., Moeller, H. V., & Archibald, K. M. (2023). Competition between phytoplankton and mixotrophs leads to metabolic character displacement. *Ecological Modelling*, *481*, 110331. https://doi.org/10.1016/j.ecolmodel.2023.110331

Crane, K. W., & Grover, J. P. (2010). Coexistence of mixotrophs, autotrophs, and heterotrophs in planktonic microbial communities. *Journal of Theoretical Biology*, *262*(3), 517–527. https://doi.org/10.1016/j.jtbi.2009.10.027

Doney, S. C., Glover, D. M., & Najjar, R. G. (1996). A new coupled, one-dimensional biological-physical model for the upper ocean: Applications to the JGOFS Bermuda Atlantic Time-series Study (BATS) site. *Deep Sea Research Part II: Topical Studies in Oceanography*, *43*(203), 591–624. https://doi.org/10.1016/0967-0645(95)00104-2

Drenkard, E. J., Stock, C. A., Ross, A. C., Teng, Y.-C., Cordero, T., Cheng, W., et al. (2025). A regional physical–biogeochemical ocean model for marine resource applications in the Northeast Pacific (MOM6-COBALT-NEP10k v1.0). *Geoscientific Model Development*, *18*(16), 5245–5290. https://doi.org/10.5194/gmd-18-5245-2025

Dutkiewic, S., Boyd, P. W., & Riebesell, U. (2020). Exploring biogeochemical and ecological redundancy in phytoplankton communities in the global ocean. *Journal of Geophysical Research: Oceans*, *27*(6), 1196–1213. https://doi.org/10.1111/gcb.15493

Edwards, K. F. (2019). Mixotrophy in nanoflagellates across environmental gradients in the ocean. *Proceedings of the National Academy of Sciences*, *116*(13), 6211–6220. https://doi.org/10.1073/pnas.1814860116

Edwards, K. F., Li, Q., McBeain, K. A., Schvarcz, C. R., & Steward, G. F. (2023). Trophic strategies explain the ocean niches of small eukaryotic phytoplankton. *Proceedings of the Royal Society B*, *290*(1991), 20222021. https://doi.org/10.1098/rspb.2022.2021

Eppley, R. E. (1972). Temperature and phytoplankton growth in the sea. *Fishery Bulletin*, *70*(4), 1063–1085.

Faure, E., Not, F., Benoiston, A.-S., Labadie, K., Bittner, L., & Ayata, S.-D. (2019). Mixotrophic protists display contrasted biogeographies in the global ocean. *The ISME Journal*, *13*(4), 1072–1083. https://doi.org/10.1038/s41396-018-0340-5

Fennel, K., Mattern, J. P., Doney, S. C., Bopp, L., Moore, A. M., Wang, B., & Yu, L. (2022). Ocean biogeochemical modelling. *Nature Reviews Methods Primers*, *2*(76), 76. https://doi.org/10.1038/s43586-022-00154-2

Fischer, R., Kitzwögerer, J., & Ptacnik, R. (2022). Light-dependent niche differentiation in two mixotrophic bacterivores. *Environmental Microbiology Reports*, *14*(4), 530–537. https://doi.org/10.1111/1758-2229.13071

Flynn, K. J., & Mitra, A. (2009). Building the "perfect beast": Modelling mixotrophic plankton. *Journal of Plankton Research*, *31*(9), 965–992. https://doi.org/10.1093/plankt/fbp044

Flynn, K. J., Mitra, A., Anestis, K., Anschütz, A. A., Calbet, A., Ferreira, G. D., et al. (2019). Mixotrophic protists and a new paradigm for marine ecology: Where does plankton research go now? *Journal of Plankton Research*, *41*(4), 375–391. https://doi.org/10.1093/plankt/fbz026

Foster, B. L. L., & Chrzanowski, T. H. (2012). The mixotrophic protist *Ochromonas danica* is an indiscriminant predator whose fitness is influenced by prey type. *Aquatic Microbial Ecology*, *68*, 1–11. https://doi.org/10.3354/ame01594

Geider, R. J., MacIntyre, H. L., & Kana, T. (1997). The role of functional traits and trade-offs in structuring phytoplankton communities: Scaling from cellular to ecosystem level. *Marine Ecology Progress Series*, *148*, 187–200.

Hansen, P. J., Bjørnsen, P. K., & Hansen, B. W. (1997). Zooplankton grazing and growth: Scaling within the 2–2,000-µm body size range. *Limnology and Oceanography*, *42*(4), 687–704. https://doi.org/10.4319/lo.1997.42.4.0687

Hartmann, M., Grob, C., Tarran, G. A., Martin, A. P., Burkill, P. H., Scanlan, D. J., & Zubkov, M. V. (2012). Mixotrophic basis of Atlantic oligotrophic ecosystems. *Proceedings of the National Academy of Sciences*, *109*(15), 5756–5760. https://doi.org/10.1073/pnas.1118179109

Hartmann, M., Zubkov, M. V., Scanlan, D. J., & Lepère, C. (2013). *In situ* interactions between photosynthetic picoeukaryotes and bacterioplankton in the Atlantic Ocean: Evidence for mixotrophy. *Environmental Microbiology Reports*, *5*(6), 835–840. https://doi.org/10.1111/1758-2229.12084

Hellweger, F. L., & Kianirad, E. (2007). Accounting for intrapopulation variability in biogeochemical models using agent-based methods. *Environmental Science Technology*, *41*(8), 2855–2860. https://doi.org/10.1021/es062046j

Hessen, D. O., Ågren, G. I., Anderson, T. R., Elser, J. J., & de Ruiter, P. C. (2004). Carbon sequestration in ecosystems: The role of stoichiometry. *Ecology*, *85*(5), 1179–1192. https://doi.org/10.1890/02-0251

Holling, C. S. (1966). The functional response of invertebrate predators to prey density. *Memoirs of the Entomological Society of Canada*, *98*(S48), 5–86. https://doi.org/10.4039/entm9848fv

Horowitz, L. W., Walters, S., Mauzerall, D. L., Emmons, L. K., Rasch, P. J., Granier, C., et al. (2003). A global simulation of tropospheric ozone and related tracers: Description and evaluation of MOZART, version 2. *Journal of Geophysical Research*, *108*(D24), 4784. https://doi.org/10.1029/2002jd002853

Jassey, V. E. J., Signarbieux, C., Hättenschwiler, S., Bragazza, L., Buttler, A., Delarue, F., et al. (2015). An unexpected role for mixotrophs in the response of peatland carbon cycling to climate warming. *Scientific Reports*, *5*(1), 16931. https://doi.org/10.1038/srep16931

Johnson, R. J., Bates, N. R., Lomas, M. W., Smith, D., Lethaby, P. J., Bakker, R., et al. (2026). *Discrete bottle samples collected at the Bermuda Atlantic Time-series Study (BATS) site in the Sargasso Sea from October 1988 through June 2025*. Biological and Chemical Oceanography Data Management Office (BCO-DMO). https://doi.org/10.26008/1912/BCO-DMO.3782.9

Kobayashi, S., Ota, Y., Harada, Y., Ebita, A., Moriya, M., Onoda, H., et al. (2015). The JRA-55 reanalysis: General specifications and basic characteristics. *Journal of the Meteorological Society of Japan. Series II*, *93*(1), 5–48. https://doi.org/10.2151/jmsj.2015-001

Leles, S. G., Bruggeman, J., Polimene, L., Blackford, J., Flynn, K. J., & Mitra, A. (2021). Differences in physiology explain succession of mixoplankton functional types and affect carbon fluxes in temperate seas. *Progress in Oceanography*, *190*, 102481. https://doi.org/10.1016/j.pocean.2020.102481

Leles, S. G., Mitra, A., Flynn, K. J., Stoecker, D. K., Hansen, P. J., Calbet, A., et al. (2017). Oceanic protists with different forms of acquired phototrophy display contrasting biogeographies and abundance. *Proceedings of the Royal Society B: Biological Sciences*, *284*(1860), 20170664. https://doi.org/10.1098/rspb.2017.0664

Leles, S. G., Polimene, L., Bruggeman, J., Blackford, J., Ciavatta, S., Mitra, A., & Flynn, K. J. (2018). Modelling mixotrophic functional diversity and implications for ecosystem function. *Journal of Plankton Research*, *40*(6), 627–642. https://doi.org/10.1093/plankt/fby044

Lepori-Bui, M., Paight, C., Eberhard, E., Mertz, C. M., & Moeller, H. V. (2022). Evidence for evolutionary adaptation of mixotrophic nanoflagellates to warmer temperatures. *Global Change Biology*, *28*(23), 7094–7107. https://doi.org/10.1111/gcb.16431

Le Quéré, C., Harrison, S. P., Colin Prentice, I., Buitenhuis, E. T., Aumont, O., Bopp, L., et al. (2005). Ecosystem dynamics based on plankton functional types for global ocean biogeochemistry models. *Global Change Biology*, *11*(11), 2016–2040. https://doi.org/10.1111/j.1365-2486.2005.1004.x

Lie, A. A. Y., Liu, Z., Terrado, R., Tatters, A. O., Heidelberg, K. B., & Caron, D. A. (2018). A tale of two mixotrophic chrysophytes: Insights into the metabolisms of two *Ochromonas* species (chrysophyceae) through a comparison of gene expression. *PLoS One*, *13*(2), e0192439. https://doi.org/10.1371/journal.pone.0192439

Liebig, J., & Playfair, L. P. (1840). In J. Liebig (Ed.), *Organic chemistry in its applications to agriculture and physiology*. Printed for Taylor and Walton.

Litchman, E., Klausmeier, C. A., Schofield, O. M., & Falkowski, P. G. (2007). The role of functional traits and trade-offs in structuring phytoplankton communities: Scaling from cellular to ecosystem level. *Ecology Letters*, *10*(12), 1170–1181. https://doi.org/10.1111/j.1461-0248.2007.01117.x

Longnecker, K., Soule, M. C. K., Swarr, G. J., Parsons, R. J., Liu, S., Johnson, W. M., et al. (2024). Seasonal and daily patterns in known dissolved metabolites in the northwestern Sargasso Sea. *Limnology and Oceanography*, *69*(3), 449–466. https://doi.org/10.1002/lno.12497

Luo, J. Y., Stock, C. A., Henschke, N., Dunne, J. P., & O'Brien, T. D. (2022). Global ecological and biogeochemical impacts of pelagic tunicates. *Progress in Oceanography*, *205*, 102822. https://doi.org/10.1016/j.pocean.2022.102822

Millette, N. C., Gast, R. J., Luo, J. Y., Moeller, H. V., Stamieszkin, K., Andersen, K. H., et al. (2023). Mixoplankton and mixotrophy: Future research priorities. *Journal of Plankton Research*, *45*(4), 576–596. https://doi.org/10.1093/plankt/fbad020

Mitra, A., Flynn, K. J., Burkholder, J. M., Berge, T., Calbet, A., Raven, J. A., et al. (2014). The role of mixotrophic protists in the biological carbon pump. *Biogeosciences*, *11*(4), 995–1005. https://doi.org/10.5194/bg-11-995-2014

Mitra, A., Flynn, K. J., Tillmann, U., Raven, J. A., Caron, D., Stoecker, D. K., et al. (2016). Defining planktonic protist functional groups on mechanisms for energy and nutrient acquisition: Incorporation of diverse mixotrophic strategies. *Protist*, *167*(2), 106–120. https://doi.org/10.1016/j.protis.2016.01.003

Moeller, H. V., Archibald, K. M., Leles, S. G., & Pfab, F. (2024). Predicting optimal mixotrophic metabolic strategies in the global ocean. *Science Advances*, *10*(50), eadr0664. https://doi.org/10.1126/sciadv.adr0664

Moeller, H. V., Neubert, M. G., & Johnson, M. D. (2019). Intraguild predation enables coexistence of competing phytoplankton in a well-mixed water column. *Ecology*, *100*(12), e02874. https://doi.org/10.1002/ecy.2874

Monod, J. (1949). The growth of bacterial cultures. *Annual Review of Microbiology*, *3*(1), 371–394. https://doi.org/10.1146/annurev.mi.03.100149.002103

O'Neill, R., DeAngelis, D., Pastor, J., Jackson, B., & Post, W. (1989). Multiple nutrient limitations in ecological models. *Ecological Modelling*, *46*(3), 147–163. https://doi.org/10.1016/0304-3800(89)90015-X

Princiotta, S. D., Smith, B. T., & Sanders, R. W. (2016). Temperature-dependent phagotrophy and phototrophy in a mixotrophic chrysophyte. *Journal of Phycology*, *52*(3), 432–440. https://doi.org/10.1111/jpy.12405

Princiotta, S. D., VanKuren, A., Williamson, C. E., Sanders, R. W., & Valiñas, M. S. (2023). Disentangling the role of light and nutrient limitation on bacterivory by mixotrophic nanoflagellates. *Journal of Phycology*, *59*(4), 785–790. https://doi.org/10.1111/jpy.13358

Puglia, M., Bibby, T. S., Wilson, J. D., & Ward, B. A. (2026). Long-term impacts of mixotrophy on ocean carbon storage: Insights from a 10 000 year global model simulation. *Biogeosciences*, *23*(1), 463–476. https://doi.org/10.5194/bg-23-463-2026

Reichl, B. G., & Hallberg, R. (2018). A simplified energetics based planetary boundary layer (ePBL) approach for ocean climate simulations. *Ocean Modelling*, *132*, 112–129. https://doi.org/10.1016/j.ocemod.2018.10.004

Ross, A. C., Stock, C. A., Adcroft, A., Curchitser, E., Hallberg, R., Harrison, M. J., et al. (2023). A high-resolution physical–biogeochemical model for marine resource applications in the Northwest Atlantic (MOM6-COBALT-NWA12 v1.0). *Geoscientific Model Development*, *16*(23), 6932–6945. https://doi.org/10.5194/gmd-16-6943-2023

Sheu, A. (2026a). alansheu2004/mixocobalt: Zenodo publication [Dataset]. *Zenodo*. https://doi.org/10.5281/ZENODO.18673182

Sheu, A. (2026b). alansheu2004/mixocobalt-data: Zenodo publication [Dataset]. *Zenodo*. https://doi.org/10.5281/ZENODO.18673195

Stock, C., & Dunne, J. (2010). Controls on the ratio of mesozooplankton production to primary production in marine ecosystems. *Deep Sea Research Part I: Oceanographic Research Papers*, *57*(1), 95–112. https://doi.org/10.1016/j.dsr.2009.10.006

Stock, C. A., Dunne, J. P., Fan, S., Ginoux, P., John, J., Krasting, J. P., et al. (2020). Ocean biogeochemistry in GFDL's Earth system model 4.1 and its response to increasing atmospheric CO_2. *Journal of Advances in Modeling Earth Systems*, *12*(10), e2019MS002043. https://doi.org/10.1029/2019ms002043

Stock, C. A., Dunne, J. P., & John, J. G. (2014). Global-scale carbon and energy flows through the marine planktonic food web: An analysis with a coupled physical–biological model. *Progress in Oceanography*, *120*, 1–28. https://doi.org/10.1016/j.pocean.2013.07.001

Stock, C. A., Powell, T. M., & Levin, S. A. (2008). Bottom–up and top–down forcing in a simple size-structured plankton dynamics model. *Journal of Marine Systems*, *74*(1), 134–152. https://doi.org/10.1016/j.jmarsys.2007.12.004

Stoecker, D. K. (1998). Conceptual models of mixotrophy in planktonic protists and some ecological and evolutionary implications. *European Journal of Protistology*, *34*(3), 281–290. https://doi.org/10.1016/s0932-4739(98)80055-2

Stoecker, D. K., Hansen, P. J., Caron, D. A., & Mitra, A. (2017). Mixotrophy in the marine plankton. *Annual Review of Marine Science*, *9*(1), 311–335. https://doi.org/10.1146/annurev-marine-010816-060617

Sunda, W. G., & Huntsman, S. A. (1995). Iron uptake and growth limitation in oceanic and coastal phytoplankton. *Marine Chemistry*, *50*(1–4), 189–206. https://doi.org/10.1016/0304-4203(95)00035-p

Tranvik, L. (1994). Colloidal and dissolved organic matter excreted by a mixotrophic flagellate during bacterivory and autotrophy. *Applied and Environmental Microbiology*, *60*(6), 1884–1888. https://doi.org/10.1128/aem.60.6.1884-1888.1994

Våge, S., Castellani, M., Giske, J., & Thingstad, T. F. (2013). Successful strategies in size structured mixotrophic food webs. *Aquatic Ecology*, *47*(3), 329–357. https://doi.org/10.1007/s10452-013-9447-y

Viljoen, J. J., Sun, X., & Brewin, R. J. W. (2024). Climate variability shifts the vertical structure of phytoplankton in the Sargasso Sea. *Nature Climate Change*, *14*(12), 1292–1298. https://doi.org/10.1038/s41558-024-02136-6

Waite, A. M., Thompson, P. A., & Harrison, P. J. (1992). Does energy control the sinking rates of marine diatoms? *Limnology and Oceanography*, *37*(3), 468–477. https://doi.org/10.4319/lo.1992.37.3.0468

Ward, B. A., Dutkiewicz, S., Barton, A. D., & Follows, M. J. (2011). Biophysical aspects of resource acquisition and competition in algal mixotrophs. *The American Naturalist*, *178*(1), 98–112. https://doi.org/10.1086/660284

Ward, B. A., & Follows, M. J. (2016). Marine mixotrophy increases trophic transfer efficiency, mean organism size, and vertical carbon flux. *Proceedings of the National Academy of Sciences*, *113*(11), 2958–2963. https://doi.org/10.1073/pnas.1517118113

Wilken, S., Choi, C. J., & Worden, A. Z. (2020). Contrasting mixotrophic lifestyles reveal different ecological niches in two closely related marine protists. *Journal of Phycology*, *56*(1), 52–67. https://doi.org/10.1111/jpy.12920

Wilken, S., Huisman, J., Naus-Wiezer, S., & Van Donk, E. (2013). Mixotrophic organisms become more heterotrophic with rising temperature. *Ecology Letters*, *16*(2), 225–233. https://doi.org/10.1111/ele.12033

Wilken, S., Schuurmans, J. M., & Matthijs, H. C. P. (2014). Do mixotrophs grow as photoheterotrophs? Photophysiological acclimation of the chrysophyte *Ochromonas danica* after feeding. *New Phytologist*, *204*(4), 882–889. https://doi.org/10.1111/nph.12975

Zhao, M., Golaz, J.-C., Held, I. M., Guo, H., Balaji, V., Benson, R., et al. (2018). The GFDL global atmosphere and land model AM4.0/LM4.0: 2. Model description, sensitivity studies, and tuning strategies. *Journal of Advances in Modeling Earth Systems*, *10*(3), 735–769. https://doi.org/10.1002/2017ms001209

Zubkov, M. V., & Tarran, G. A. (2008). High bacterivory by the smallest phytoplankton in the North Atlantic Ocean. *Nature*, *455*(7210), 224–226. https://doi.org/10.1038/nature07236